JACS
JOURNAL OF THE AMERICAN CHEMICAL SOCIETY
Article
Cite This: J. Am. Chem. Soc. 2019, 141, 17875−17883
pubs.acs.org/JACS

Cooperative Stabilization of the [Pyridinium-CO_2-Co] Adduct on a Metal−Organic Layer Enhances Electrocatalytic CO_2 Reduction

Ying Guo,[†,§] Wenjie Shi,[†,§] Huijuan Yang,[†] Quanfeng He,[†] Zhongming Zeng,[†] Jin-yu Ye,[†] Xinru He,[†] Ruiyun Huang,[†] Cheng Wang,*[,†] and Wenbin Lin[‡]

[†]State Key Laboratory of Physical Chemistry of Solid Surfaces, iCHEM, College of Chemistry and Chemical Engineering, Xiamen University, Xiamen 361005, P.R. China

[‡]Department of Chemistry, The University of Chicago, 929 East 57th Street, Chicago, Illinois 60637, United States

Supporting Information

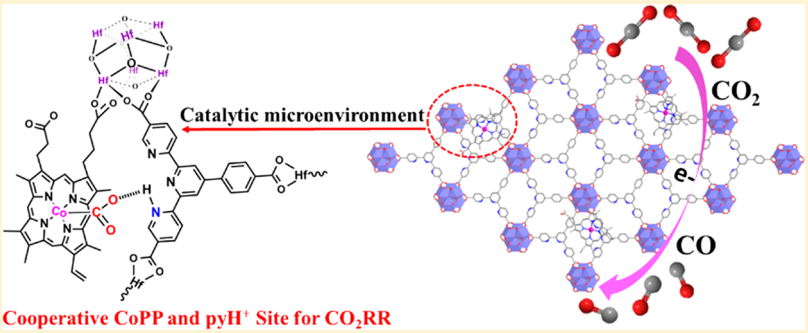

ABSTRACT: Pyridinium has been shown to be a cocatalyst for the electrochemical reduction of CO_2 on metal and semiconductor electrodes, but its exact role has been difficult to elucidate. In this work, we create cooperative cobalt-protoporphyrin (CoPP) and pyridine/pyridinium (py/pyH$^+$) catalytic sites on metal−organic layers (MOLs) for an electrocatalytic CO_2 reduction reaction (CO_2RR). Constructed from $[Hf_6(\mu_3\text{-}O)_4(\mu_3\text{-}OH)_4(HCO_2)_6]$ secondary building units (SBUs) and terpyridine-based tricarboxylate ligands, the MOL was postsynthetically functionalized with CoPP via carboxylate exchange with formate capping groups. The CoPP group and the pyridinium (pyH$^+$) moiety on the MOL coactivate CO_2 by forming the [pyH$^+$-$^-$O$_2$C-CoPP] adduct, which enhances the CO_2RR and suppresses hydrogen evolution to afford a high CO/H_2 selectivity of 11.8. Cooperative stabilization of the [pyH$^+$-$^-$O$_2$C-CoPP] intermediate led to a catalytic current density of 1314 mA/mgCo for CO production at −0.86 V_{RHE}, which corresponds to a turnover frequency of 0.4 s^{-1}.

INTRODUCTION

Converting CO_2 into useful chemicals using electricity from solar and other renewable energy sources is one of the most active areas of current research.[1−6] To achieve high faradaic efficiency (FE) in a CO_2 reduction reaction (CO_2RR), the competing hydrogen evolution reaction (HER) must be suppressed at the requisite negative potential for the CO_2RR.[7,8] The pyridine/pyridinium (py/pyH$^+$) species has been reported to be a cocatalyst for the electrochemical CO_2RR on various metal and semiconductor electrodes.[9−13] Similarly, nitrogen-doped carbons (N-Cs) with pyridinic nitrogen are effective for the CO_2RR with high FEs.[14,15] The exact role of py/pyH$^+$ is still under investigation.[16−20]

For example, theoretical calculations revealed 1,2-dihydropyridine (pyH_2) as a possible intermediate mimicking NADPH in natural photosynthesis to transfer a hydride to CO_2 for its reduction, but experimental attempts to directly detect this intermediate or related D/H exchange species in isotope experiments have failed.[17] On the other hand, the electrogeneration of the pyridinyl radical (pyH$^•$) was also proposed as the electron shuttle for CO_2 reduction. Such π-radicals were observed by electron paramagnetic spectroscopy (EPR) and UV−vis spectroscopy for 4,4′-bipyridinium in aqueous solution using a Pt working electrode, but the calculated redox potential of pyH$^•$ appears to be too negative for its participation in the reaction.[19] In an alternative explanation, pyridinium can assist the formation of hydride on the electrode surface to steer selectivity toward the CO_2RR by modulating the microenvironment around the catalytic centers on the electrode.[19]

If the promoting effect of py/pyH$^+$ can be generalized to molecular CO_2RR catalysts, then we conjectured that molecular materials with well-defined catalytic sites would be ideally suited for pinpointing the role of py/pyH$^+$ in the CO_2RR. Herein we report the study of py/pyH$^+$ in enhancing the CO_2RR by a cobalt−porphyrin electrocatalyst in a metal−organic layer (MOL).

As a monolayer version of 2D metal−organic frameworks (MOFs), MOLs have recently been developed as a novel class

Received: August 26, 2019
Published: October 11, 2019

DOI: 10.1021/jacs.9b09227
J. Am. Chem. Soc. 2019, 141, 17875−17883

of functional molecular materials.[21−23] MOLs are ideally suited for electrocatalysis because their ultrathin nature overcomes the conductivity constraint in MOFs.[24] The distances for electron migration and counterion movement are quite short through a monolayer, enabling the use of MOLs as effective electrocatalysts.[25] MOLs also allow for controlling the microenvironment around catalytic centers through surface modification of the secondary building units (SBUs).[26]

In this work, we used MOLs as a 2D scaffold to tune the microenvironment of the Co-protoporphyrin (CoPP) electrocatalyst for the CO_2RR in aqueous media. CoPP was postsynthetically installed on the $[Hf_6(\mu_3\text{-}O)_4(\mu_3\text{-}OH)_4(HCO_2)_6]$ SBUs of BTB-MOL and TPY-MOL built from triangular benzenetribenzoate (BTB) and 4′-(4-benzoate)-(2,2′,2″-terpyridine)-5,5″-dicarboxylate (TPY) linkers, respectively,[26] via carboxylate exchange with formate capping groups on the MOLs (Figure 1). Changing the microenvironment around CoPP from phenyl rings in BTB to py moieties in TPY significantly enhanced the electrocatalytic CO_2RR, increasing the CO/H_2 current density ratio from 2.7 in BTB-MOL-CoPP to 11.8 in TPY-MOL-CoPP at an electrolysis potential of −0.86 V vs the reversible hydrogen electrode (V_{RHE}).

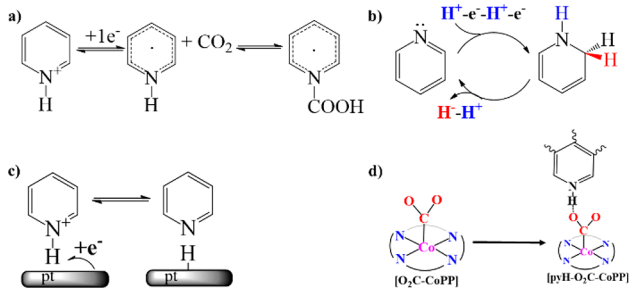

Figure 1. Different views on the function of the py/pyH$^+$ species in the CO_2RR: (a) Pyridinium reduction by one electron, forming the pyridinyl radical, followed by its reaction with CO_2 to form a radical carbamate.[19] (b) Formation of 1,2-dihydropyridine (PyH_2) from PyH^0 via successive $1H^+/1e^-$ transfers.[17] (c) Inner-sphere reduction of a pyrH$^+$-bound proton on a Pt electrode to form a surface hydride.[19] (d) Cooperative activation of CO_2 by CoPP and pyH$^+$ in this work.

RESULTS AND DISCUSSION

Catalyst Synthesis and Characterization. BTB-MOL and TPY-MOL with compositions of $[Hf_6(\mu_3\text{-}O)_4(\mu_3\text{-}OH)_4(HCO_2)_6(L)_2]$ (L = BTB and TPY, respectively) were synthesized following our previous report.[23] The MOLs were then functionalized with CoPP in DMF at 60 °C. The methylene bridge between the carboxylate linker and the porphyrin moiety in CoPP lends flexibility to the structure to better accommodate CO_2 as a substrate. Such flexible linkages are widely utilized in many enzymes to allow for an "induced fit" between the catalytic center and the substrate.[27,28] We hypothesized that these structural features would lead to cooperativity between TPY and CoPP in the electrocatalytic CO_2RR.

The MOLs appeared as wrinkled ultrathin films by transmission electron microscopy (TEM) (Figure 2a, Figures S1 and S2). Their powder X-ray diffraction (PXRD) patterns were consistent with the structure of the 3,6-connected 2D net of alternatively linked tricarboxylate ligands and Hf_6 SBUs with the kgd topology (Figure 2b, Figure S3). Atomic force microscopy (AFM) showed a thickness of 1.2 ± 0.2 nm for the as-synthesized TPY-MOL (Figure S1), which corresponds to the van der Waals diameter of Hf_6 SBUs and suggests the monolayer structure of the MOL.

The amounts of adsorbed CoPP were quantified to be 8.4 wt % for BTB-MOL-CoPP and 5.5 wt % for TPY-MOL-CoPP by UV−vis spectroscopy (Figure S4), which correspond to CoPP/Hf_6 SBU ratios of 0.32 and 0.17, respectively (Table S1). TEM images and PXRD patterns of the modified samples were very similar to those of the as-synthesized MOLs, confirming structural stability during the modification (Figure 2a,b, Figures S1−S3). PXRD patterns of TPY-MOL-CoPP recovered from suspensions in an N_2-saturated 0.1 M buffer solution of NaH_2PO_4/Na_2HPO_4 and a CO_2-saturated 0.1 M $NaHCO_3$ solution confirmed the structural stability in the electrolytic solution (Figure S5). AFM measurements of TPY-

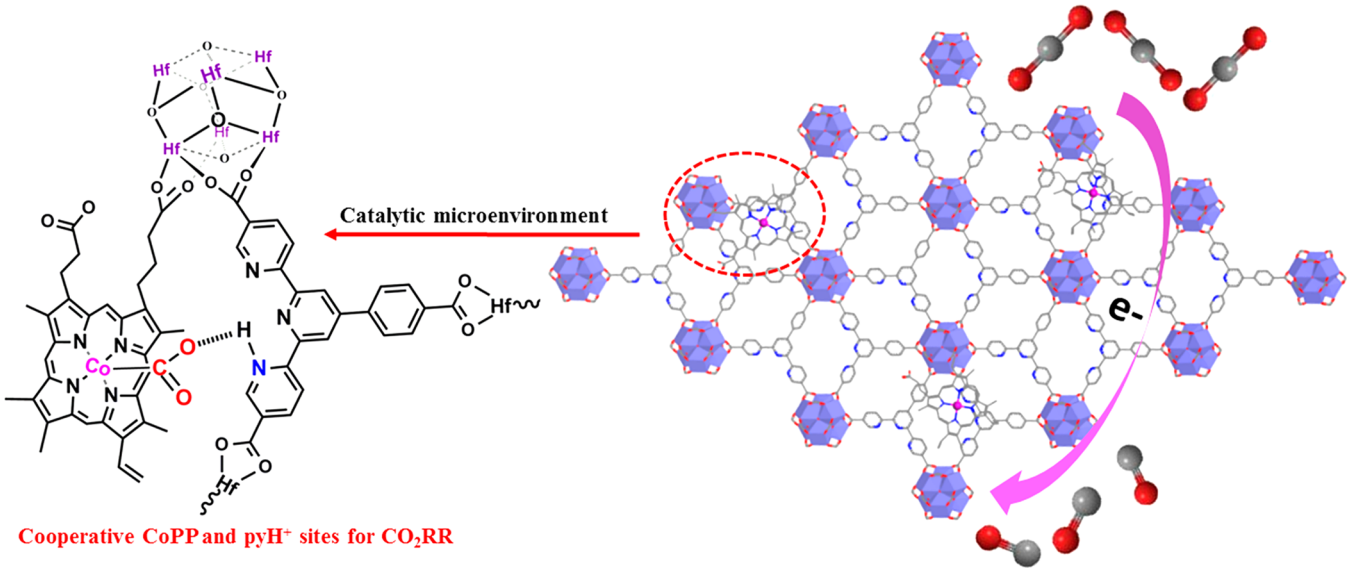

Figure 2. Schematic showing the structure of TPY-MOL-CoPP and the cooperative activation of CO_2 by CoPP and pyH$^+$.

DOI: 10.1021/jacs.9b09227
J. Am. Chem. Soc. 2019, 141, 17875−17883

MOL-CoPP gave a thickness of 1.8 ± 0.2 nm (Figure 2c), which is slightly thicker than that of the unmodified one (1.2 ± 0.2 nm) as a result of the steric bulk of CoPP.

It is important to consider if the pyridine moiety on TPY can directly coordinate to the Co center on CoPP in TPY-MOL-CoPP. The structural modeling of the CoPP catalytic center by Materials Studio software showed that the steric bulk of the terpyridine and the MOL SBUs prevents such a coordination (Figure 3f). Molecular mechanics optimization (using a universal force field for MOF) of a structural model beginning with a forced coordination between Co and N on the terpyridine led to the cleavage of the coordination bond as a result of the steric repulsion between the CoPP and TPY moieties. The resulting structure has the shortest Co−N distance of 4.75 Å, which is beyond the range of a coordination bond (Figures S6 and S7). Furthermore, a careful study of the UV−vis spectra of a series of MOL-CoPP composites also ruled out such a coordination (Figure 3e). The UV−vis spectrum of the pyridine-treated CoPP molecule (CoPP-py) or BTB-MOL-CoPP sample (BTB-MOL-CoPP-py) showed an additional shoulder at around 400 nm toward the blue side of the Soret absorption band of CoPP in BTB-MOL-CoPP, which is characteristic of the CoPP-py moiety. However, this spectrum feature is absent in the UV−vis of TPY-MOL-CoPP. On the other hand, treating TPY-MOL-CoPP with additional free pyridine generates features similar to those of CoPP-py in the UV−vis spectrum. All of these observations support a lack of pyridine coordination to Co in the TPY-MOL-CoPP sample.

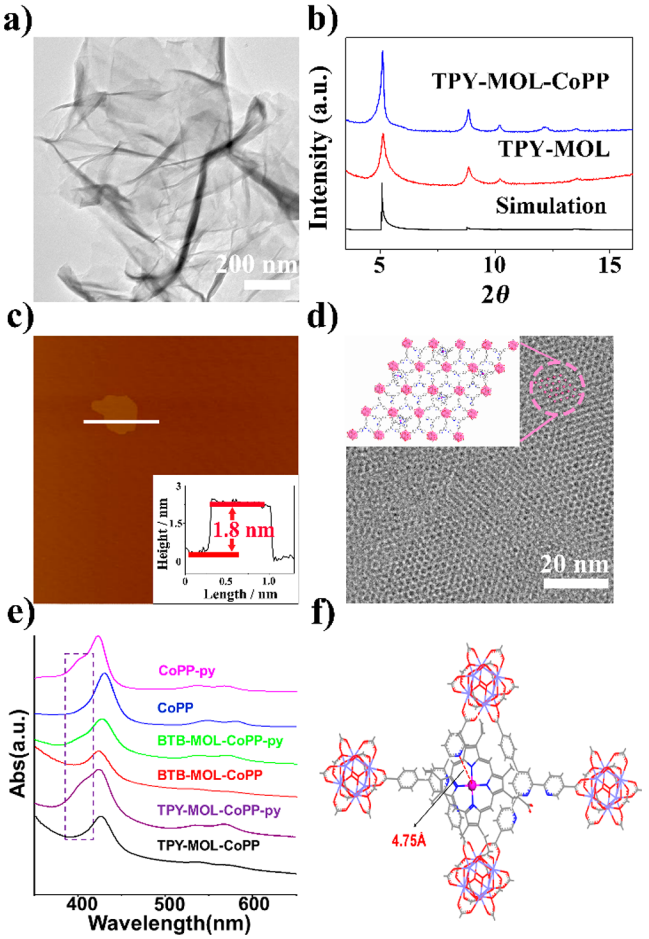

Figure 3. (a) TEM images of TPY-MOL-CoPP. (b) PXRD patterns of TPY-MOL and TPY-MOL-CoPP. (c) AFM and (d) HRTEM images of TPY-MOL-CoPP. (e) UV−vis spectroscopy of CoPP, CoPP coordinated with pyridine, BTB-MOL-CoPP, BTB-MOL-CoPP with additional pyridine, TPY-MOL-CoPP, and TPY-MOL-CoPP with additional pyridine. (f) Optimization of a structural model of TPY-MOL-CoPP showing the closest distance between Co and N on the terpyridine.

Catalytic Activity. The CO_2RR activities of the MOL catalysts were measured in a CO_2-saturated aqueous solution of 0.1 M $NaHCO_3$ in an airtight H-type cell with Nafion membranes separating working and counter electrodes. The MOLs were stable in the buffer solution as revealed by the retention of their PXRD patterns (Figure S5). The MOL-CoPP samples were loaded onto carbon cloth by drop-drying. Electrolysis was performed in the potential range of −0.56 to −0.86 V_{RHE}. CO and H_2 were detected by online gas chromatography (GC). No liquid products were detected by ^{1}H NMR spectra taken at the completion of each electrolysis. The catalytic current densities for CO (j_{CO}) and H_2 (j_{H_2}) were calculated according to the amounts of H_2 and CO generated with respect to the quantities of charge passed in electrolysis. The faradaic efficiencies (FEs) were calculated as the ratios between the partial current densities and the total current densities (j_{total}).

At −0.86 V_{RHE}, BTB-MOL-CoPP had a j_{CO} of 923 mA/mg (Figure S8) on a per cobalt basis with a j_{CO}/j_{H_2} ratio of 2.7, and TPY-MOL-CoPP exhibited a j_{CO} of 1314 mA/mg with a much higher j_{CO}/j_{H_2} ratio of 11.8 (Figure 4a). TPY-MOL-CoPP had a CO-FE of 92.2% (Figure 4a) and a turnover frequency of 0.40 s^{-1}. Such activity is much higher than those of many other

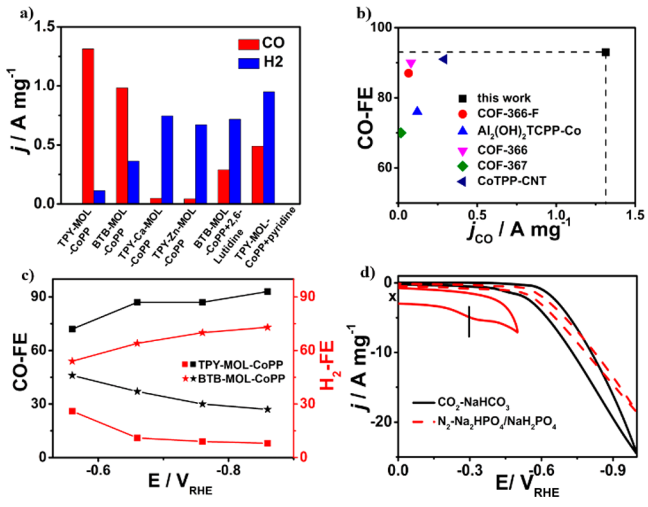

Figure 4. (a) Current densities per milligram of cobalt for different MOL-CoPP catalysts at an applied potential of −0.86 V_{RHE} in a CO_2-saturated 0.1 M $NaHCO_3$ aqueous solution. (b) Comparison of the CO_2RR catalytic performances of different Co-porphyrin-based catalysts. The *x* axis represents the current density on a per milligram of cobalt basis, and the *y* axis represents CO-FE. (c) Faradaic efficiency for CO and H_2 vs the electrolysis potential for different catalysts in CO_2-saturated 0.1 M $NaHCO_3$. (d) Cathodic wave (CV) of TPY-MOL-CoPP in CO_2-saturated 0.1 M $NaHCO_3$ (black solid lines) and in N_2-saturated 0.1 M NaH_2PO_4/Na_2HPO_4 (red dashed lines). Enlarged Cathodic wave (CV) of TPY-MOL-CoPP in N_2-saturated 0.1 M NaH_2PO_4/Na_2HPO_4 at a scan rate of 200 mV/s (red solid lines).

DOI: 10.1021/jacs.9b09227
J. Am. Chem. Soc. 2019, 141, 17875−17883

porphyrin-based electrocatalysts for CO_2 conversion to CO (Figure 4b).[2,29−31] At lower potentials, TPY-MOL-CoPP also had higher CO-FE than did BTB-MOL-CoPP (Figure 4c). Control experiments using TPY-MOL and BTB-MOL without CoPP functionalization showed only HER (Figure S9), demonstrating that CoPP is the catalytic center.

The promoting effect of the TPY ligand for the CO_2RR was verified in a poisoning experiment by coordinating the TPY site with Zn^{2+} or Ca^{2+}, which significantly reduced CO-FE from 92.2 to 6 and 8%, respectively (Figure 4a). Consistent with our analysis, the promoting effect of TPY is not due to pyridine coordination to the Co center in CoPP because the addition of pyridine to the solution led to a significantly reduced CO-FE to 29% (Figure 4a). The promoting effect of TPY was observed at all potentials (Figure 4c, Figures S8 and S10).

To understand the origin of the CO_2RR vs HER selectivity, we compared electrocatalysis in a CO_2-saturated aqueous solution of 0.1 M $NaHCO_3$ at pH 6.8 and in N_2-saturated NaH_2PO_4/Na_2HPO_4 buffer solutions at pH 6.8. Both TPY-MOL-CoPP and BTB-MOL-CoPP had higher current densities in CO_2-saturated solutions ($j_{in\ CO_2}$) than in N_2-saturated solutions ($j_{in\ N_2}$). The $j_{in\ CO_2}$ values contain current densities for both the HER and CO_2RR, and the $j_{in\ N_2}$ values are entirely from HER (Figure S11, Table S2). However, the $(j_{in\ CO_2} - j_{in\ N_2})/j_{in\ CO_2}$ ratios are much lower than the FEs for the CO_2RR at various potentials for both MOL catalysts. This result suggests that HER is suppressed in the presence of the CO_2RR. Consistent with this, the current densities for HER (j_{H_2}) in CO_2-saturated solution are much lower than those in N_2-saturated solution (Tables S2 and S3). This suppression of HER is likely due to the CO_2RR and HER competing for the same catalytic sites. We note that it may also result from the higher local pH in the CO_2RR with $CO_2/HCO_3^-/CO_3^{2-}$ buffer than in the N_2 atmosphere with NaH_2PO_4/Na_2HPO_4 buffer. The j_{H_2} value for TPY-MOL-CoPP is similar to the background current density of the carbon cloth without loading any catalyst. The HER of TPY-MOL-CoPP under a CO_2 atmosphere thus mainly comes from the carbon cloth, indicating that the intrinsic CO/H_2 selectivity of the CoPP site in TPY-MOL-CoPP should be even higher than the measured value of 11.8.

A reductive peak at ~−0.28 V_{RHE} can also be found on the CV scan of TPY-MOL-CoPP under the N_2 atmosphere with NaH_2PO_4/Na_2HPO_4 buffer when the scan rate was 200 mV/s (Figure 4d, Figure S12). This peak is assigned to the reduction of $[CoPP]^0$ to $[CoPP]^-$. The CO_2RR and HER both occur at more negative onset potentials than −0.28 V_{RHE}, which should correspond to the potentials for the injection of the second electrons.

Local pH and Mass Transport in Electrolysis. To reveal the function of the pyridine promoter, we first examined the possibility for the pyridine group to affect local pH or the mass transport of CO_2.

As a result of a fast consumption of proton or generation of hydroxide in the electrocatalytic CO_2RR and HER processes, the solution around the electrode surface can exhibit significantly higher local pH than the bulk solution (Figure 5a). Both CO_2RR and HER processes consume one proton or generate one hydroxide while obtaining one electron. We can thus build up a general relationship between the local pH and

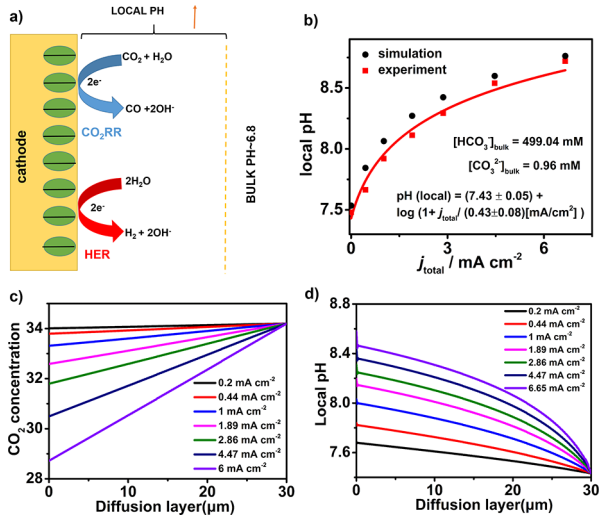

Figure 5. (a) Buildup of local pH near the electrode due to the CO_2RR and HER. (b) Fitted equation of the local pH in the CO_2RR using COMSOL and the experimental local pH from ref 33 together with the fitting from eq 4, with 0.5 M HCO_3^- in the electrolytes. (c) CO_2 concentration distribution under different steady-state conditions from COMSOL simulation. (d) Local pH distribution under steady-state conditions from the COMSOL simulation.

the catalytic current density with a given concentration of the buffering species.

The CO_2/HCO_3^- pair is not an efficient buffer pair because of its slow kinetics in proton transfer. The rate of CO_2 dissociation to generate HCO_3^- and a proton is around 0.0371 s^{-1},[32] which can give local protons at a maximum rate of 3.7×10^{-9} mol cm^{-2} s^{-1} considering a liquid layer of 30 μm thickness around the electrode and a saturated CO_2 concentration of ~34 mM (thus 1×10^{-7} mol cm^{-2} of CO_2 near the electrode) as a "local" reservoir. This possible maximum rate is still much lower than the rate of proton consumption in the electrocatalytic CO_2RR with a current density of >1 mA/cm^2 (~1×10^{-8} mol cm^{-2} s^{-1} proton consumption). As a result, we can ignore the conversion of CO_2 to HCO_3^- in the "local" environment around the electrode as a proton generation source in the electrocatalysis in a rough estimation. Similarly, the rate of water dissociation to produce H^+ and OH^- is not fast enough (2.4×10^{-5} M s^{-1}) to provide protons (7.2×10^{-11} mol cm^{-2} s^{-1} proton generation rate in a 30 μm liquid layer) for proton consumption in electrolysis.

At steady state, the consumed proton at the electrode should be provided by the diffusion and the equilibrium of hydronium (H_3O^+), hydroxide (OH^-), and bicarbonate/carbonate (HCO_3^-/CO_3^{2-}). Because of the low bulk concentration of H_3O^+ ($10^{-6.8}$ M) and OH^- ($10^{-7.2}$ M) in the bulk solution at pH 6.8 as compared to the concentration of HCO_3^- (0.1 M), the contribution from H_3O^+ and OH^- diffusion can be ignored. The conversion between HCO_3^- and CO_3^{2-} is fast enough with a rate constant of 59.44 s^{-1}[32] that corresponds to a maximum local proton generation rate of 1.8×10^{-5} mol cm^{-2} s^{-1} considering a liquid layer of 30 μm thickness. We can thus simplify the analysis by considering HCO_3^- to be the only proton carrier in the reaction.

Combining the mass conservation of proton under the steady-state condition with Fick's diffusion law, we can obtain

DOI: 10.1021/jacs.9b09227
J. Am. Chem. Soc. 2019, 141, 17875−17883

$$\frac{j_{total}}{F} = -D_{HCO_3^-}\frac{\partial[HCO_3^-]}{\partial x}\bigg|_{x=0} = D_{HCO_3^-}\frac{[HCO_3^-]_{bulk} - [HCO_3^-]_{local}}{l} \quad (1)$$

where the D is the diffusivity of bicarbonate and l is the effective thickness of the diffusing layer.

Because we ignored the hydration of CO_2 in the proton balance, the sum of the flux of bicarbonate and carbonate is a constant at steady state because of the conservation of mass.

$$D_{HCO_3^-}\frac{\partial[HCO_3^-]}{\partial x} + D_{CO_3^{2-}}\frac{\partial[CO_3^{2-}]}{\partial x} = 0 \quad (2)$$

Combining these conservation of mass equations with the equilibrium equation between the carbonate and bicarbonate, we have

$$\frac{[HCO_3^-]_{local}}{[CO_3^{2-}]_{local}} = \frac{[H^+]_{local}}{K_{a2}} \quad (3)$$

We can obtain (see the SI for more details)

$$pH_{local} = pH_{bulk} + \log\left(1 + \frac{j_{total}}{j_d}\right) \quad (4)$$

where

$$j_d = F\frac{D_{CO_3^{2-}}[CO_3^{2-}]_{bulk}}{l} \quad (5)$$

The local pH of the CO_2RR with stirring in the solution has been measured by Xu et al. using electrochemical diffuse reflectance infrared Fourier transform spectroscopy (DRIFTS),[33] which estimates the local pH from the concentration ratio between the carbonate and bicarbonate. Fitting the equation with data from ref 33 gives an effective diffusing layer thickness of l = 31 μm (Figure 5b). Such a diffusing layer thickness is reasonable for a system with mechanical stirring in the solution.[34]

The rate of CO_2 mass transport can be estimated by a $^{13}CO_2$ exchange experiment. $^{13}CO_2$ gas was used to fill the headspace of the vial with 0.1 M $NaH^{12}CO_3$ electrolyte under vigorous stirring either in the presence or in the absence of TPY-MOL-CoPP in the solution. Online mass spectrometry (MS) measured the $^{13}CO_2/^{12}CO_2$ ratio in the headspace as a function of time (Figure S13), the kinetic curve of which reflects the rate of CO_2 transfer between the gas and liquid phases to give a specific mass transport coefficient of (0.0015 ± 0.0002) s^{-1} that corresponds to a CO_2 feeding rate of ~1.5 × 10^{-6} mol s^{-1}, giving a total solution volume of 30 mL, far exceeding the CO_2 consumption rate at the electrode (~1 × 10^{-8} mol s^{-1} for a current density of 1 mA/cm^2 and an electrode area of 1 cm^2). This proves that the CO_2 transport from the gas phase to the liquid phase does not present a limitation on the electrolysis, and we can thus assume a saturated CO_2 concentration of 34 mM in the bulk solution. Combining this concentration with the CO_2 diffusivity of 1.9 × 10^{-9} m^2/s and a required CO_2 transport flux of 1 × 10^{-8} mol cm^{-2} s^{-1} (1 mA/cm^2) to the electrode, the CO_2 concentration at the electrode should still be 32.4 mM assuming a diffusing layer of 30 μm in thickness. As a result, the CO_2 transport is not likely to be a limitation of the CO_2RR in the current experimental setup.

To validate the above assumptions in deriving the equation for local pH and to corroborate with the CO_2 diffusion analysis, we also performed numerical simulations with COMSOL Multiphysics v4.3b software[32,35] using the diffusivities of different species and the reaction rates among them (without adopting the above assumption of ignoring the CO_2 dissociation process). The dominant role of HCO_3^- as the H carrier was confirmed in the simulation, and the local pH values obtained from the simulation are very similar to those predicted from eq 4 (Figure 5b–d).

A typical local pH of ~8.0 was obtained for the CO_2RR at a current density of ~1 mA/cm^2 and a $NaHCO_3$ concentration of 0.1 M in the CO_2-saturated solution. This local pH is well above the pK_a of pyridinium/pyridine of 4–6. The buffering effect of pyridinium/pyridine at the local pH is thus negligible because all of the free pyridine should be in the deprotonated form. Because these pyridine/pyridinium moieties are fixed on the electrode surface without the continuous transportation of pyridinium from the bulk solution, they cannot serve as a bulk pyridine/pyridinium buffer and have no effect on the local pH at steady state.

Kinetics Studies and the Apparent Rate Law. We have changed the partial pressure of CO_2 and the concentration of HCO_3^- in the solution to study the dependence of the CO and H_2 current densities on these parameters. Different amounts of NaCl or Na_2HPO_4 were also added to the solution in addition to $NaHCO_3$ to keep the Na^+ concentration the same in all of the tests (Tables S4 and S5). We must note that the change in the CO_2 partial pressure and the HCO_3^- concentration also changes the bulk pH of the system and the local pH around the catalytic electrode. The addition of Na_2HPO_4 leads to additional buffering pair $H_2PO_4^-/HPO_4^{2-}$ with a pK_a of 7.21 to affect both the bulk and local pH. The pH of the bulk solution ranges from 6.42 to 7.42 in these experiments, and the local pH around the electrode ranges from 6.42 to 9.32 according to eq 4.

The CO current density increases with both increasing CO_2 partial pressure and increasing HCO_3^- concentration (Figure 6a,b). We can obtain an apparent rate law of the CO_2RR (Figure 6c,d) for the TPY-MOL-CoPP catalyst as

$$j_{CO} = 11\,900\ mA\ mg^{-1}\ M^{-1}([HCO_3^-] + 0.041\ M)\frac{[CO_2]}{[CO_2] + 0.011\ M} \quad (6)$$

The apparent rate law of the CO_2RR for the BTB-MOL-CoPP catalyst is

$$j_{CO} = 7000\ mA\ mg^{-1}\ M^{-1}([HCO_3^-] + 0.059\ M) \times \frac{[CO_2]}{[CO_2] + \frac{[H^+]_{local}}{10^{-4.9}} + 0.017\ M} \quad (7)$$

These two similar rate laws of TPY-MOL-CoPP and BTB-MOL-CoPP indicate that the pyridine moiety in TPY-MOL-CoPP may not change the catalytic path of the CoPP catalyst but significantly tunes the reaction rate or the equilibrium among related species in the elementary steps. The dependence of the reaction rate on the local concentration of bicarbonate suggests that there is a HCO_3^--assisted path acting as the major turnover path when the HCO_3^- concentration is >0.1 M. The Langmuir-type dependence on the CO_2 concentration suggests an equilibrium of an active CO_2-adsorbed species with other CO_2-related species in the system. This species is likely to be the one before the rate-determining step (RDS), in other words, the resting state of the catalyst-CO_2 assembly.

DOI: 10.1021/jacs.9b09227
J. Am. Chem. Soc. 2019, 141, 17875–17883

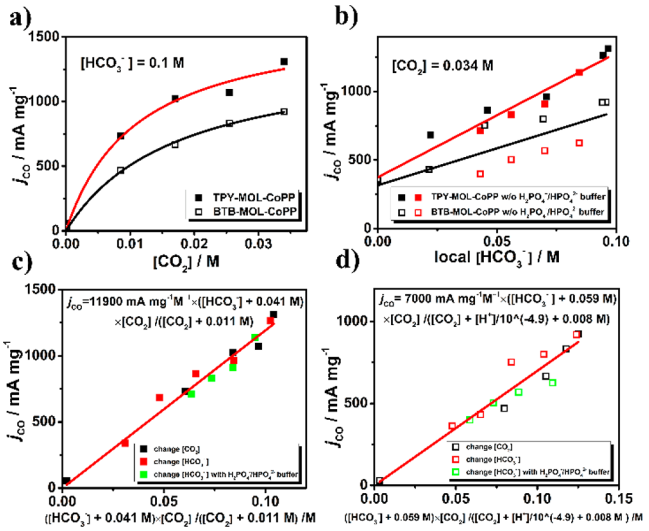

Figure 6. (a) Dependence of CO current density on the CO_2 concentration (changing p_{CO_2}) in the bulk solution at a constant potential of −0.86 V_{RHE} for TPY-MOL-CoPP and BTB-MOL-CoPP. (b) Dependence of the CO current density on the HCO_3^- concentration at a constant potential of −0.86 V_{RHE} for TPY-MOL-CoPP and BTB-MOL-CoPP (black squares, different $H_2PO_4^-/HPO_4^{2-}$ buffer concentrations for TPY-MOL-CoPP; red squares, tuning the HCO_3^- concentration without adding $H_2PO_4^-/HPO_4^{2-}$ buffer for TPY-MOL-CoPP; open black squares, different $H_2PO_4^-/HPO_4^{2-}$ buffer concentrations for BTB-MOL-CoPP; and open red squares, tuning the HCO_3^- concentration without adding $H_2PO_4^-/HPO_4^{2-}$ buffer for BTB-MOL-CoPP). (c, d) Rate laws of the CO_2RR for the TPY-MOL-CoPP and BTB-MOL-CoPP catalysts, with experimental data from tuning the CO_2 concentration by changing p_{CO_2} (black), tuning the HCO_3^- concentration (red), and adding different concentrations of the $H_2PO_4^-/HPO_4^{2-}$ buffer (green).

In Situ Electrochemical Diffuse Reflectance Infrared Fourier Transform Spectroscopy. We then performed in situ electrochemical DRIFTS in an attempt to capture the resting-state species before the RDS and to gain further insight into the role of py/pyH^+ in the CO_2RR (Figure 7a). When the potential was scanned in the negative direction, the differential spectra of TPY-MOL-CoPP (using the spectra at 0.14 V_{RHE} as a reference) under a CO_2 atmosphere (CO_2/$NaHCO_3$, 0.1 M, pH 6.8) showed the appearance of a positive peak at 1438

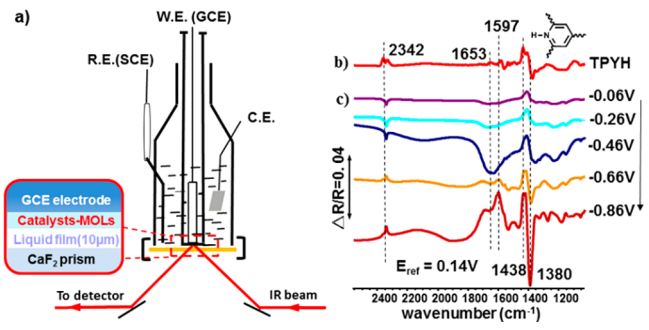

Figure 7. (a) Schematic of the thin-layer IR cell for the in situ DRIFTS study. (b) IR spectra of TPY-MOL (in H_2O, black line) and $TPYH^+$-MOL (pH 4.0 with $HClO_4$, red line). (c) DRIFTS of TPY-MOL-CoPP in the potential scan range of −0.06 to −0.86 V_{RHE} in a CO_2-saturated aqueous solution of 0.1 M $NaHCO_3$. The reference spectrum was taken at 0.14 V_{RHE}.

cm^{-1} and a negative peak at 1380 cm^{-1} (Figure 7c), which are assigned to the loss of pyridine due to the formation of pyridinium. Such an assignment is confirmed by the very similar DRIFTS spectrum of protonating TPY-MOL-CoPP with HCl (Figure 4b). This pyH^+ feature was not observed for either TPY-MOL-CoPP under an N_2 atmosphere (Figure S14) or BTB-MOL-CoPP under a CO_2 atmosphere (Figure S15). The positive peaks near 2342 and 1597 cm^{-1} were assigned to the consumption of CO_2 and HCO_3^- in the reaction. Only weak IR signals at 1653 cm^{-1} due to the formation of $[CoPP]^-$ or $[HCoPP]^0$ were observed in those control experiments (Figures S14–S16, Table S6). TPY-MOL without CoPP did not give any differential DRIFTS signal in the potential scan. On the basis of these results, we propose the formation of $[pyH^+\text{-}^-O_2C\text{-}CoPP]^0$ as a key intermediate for TPY-promoted CO_2 activation and reduction.

The signal due to pyridinium began to show up at the scanning potential of around −0.26 V, which coincides with the potential for the reduction of $[CoPP]^0$ to $[CoPP]^-$. This is consistent with the formation of $[pyH^+\text{-}^-O_2C\text{-}CoPP]^0$ from $[CoPP]^-$, CO_2, and the preassembled pyridine moiety. The DRIFTS signal continues to become more and more prominent upon scanning to more negative potentials. This may indicate the formation of the reduced $[pyH^+\text{-}^-O_2C\text{-}CoPP]^-$ species with a DRIFTS signal at similar positions but possibly different intensities as compared to that of $[pyH^+\text{-}^-O_2C\text{-}CoPP]^0$ (Table S7).

Theoretical Studies and the Catalytic Cycle. We performed theoretical calculations using density functional theory (DFT) in order to reveal key steps for the catalytic cycle (Figures S17–S19, Table S9). The pathways for the Co-porphyrin catalyzed CO_2RR were established by the works of Koper, Nielsen, and Leung.[36−38] $[CoPP]^0$ is first reduced to $[CoPP]^-$[39] (V_{RHE} = −0.4 V by DFT [Figure S20, Tables S8 and S9] and −0.28 V from experiment [Figure S12]) and then protonated to $[H\text{-}CoPP]^0$ or an adduct was formed with CO_2 to yield $[HO_2C\text{-}CoPP]^0$. A further one-electron reduction of $[H\text{-}CoPP]^0$ to $[H\text{-}CoPP]^-$ followed by protonation generates H_2 for HER (V_{RHE} = +0.4 V by DFT, Figures S20 and S21), whereas a one-electron reduction of $[HO_2C\text{-}CoPP]^0$ (V_{RHE} = 0.4 V by DFT) followed by the cleavage of a C−O bond leads to the formation of CO for the CO_2RR (Figure 8a, Figure S22).[40]

In this catalytic cycle, there is a significant barrier to the protonation of adsorbed CO_2, as indicated by the calculated pK_a of 4.2 for $[HO_2C\text{-}CoPP]^0$, which is disfavored at neutral pH. As a result, the HER path can compete with the CO_2RR for the BTB-MOL-CoPP catalyst because of the more favorable formation of the $[HCoPP]^0$ intermediate. A proton-coupled electron transfer pathway at higher overpotential is favored to produce $[HO_2C\text{-}CoPP]^-$ (Figure 8a). In contrast, the pyridine moiety adjacent to the CoPP center in TPY-MOL-CoPP stabilizes the protonated species $[pyH\text{-}O_2C\text{-}CoPP]^0$. Further injection of the second electron followed by C−O cleavage leads to the CO generation. The proton-coupled electron transfer can still form $[pyH\text{-}O_2C\text{-}CoPP]^-$, but the stepwise protonation/electron transfer path should be competitive for the TPY-MOL-CoPP catalyst.

The preassembled cooperative site is critical to pyridine in stabilizing the $[pyH\text{-}O_2C\text{-}CoPP]^{0/-}$ intermediate. Free pyridine in solution does not promote the formation of such an adduct because of entropy loss of the free pyridine in the process as indicated by DFT calculation (Figure S23). In contrast, the

DOI: 10.1021/jacs.9b09227
J. Am. Chem. Soc. 2019, 141, 17875−17883

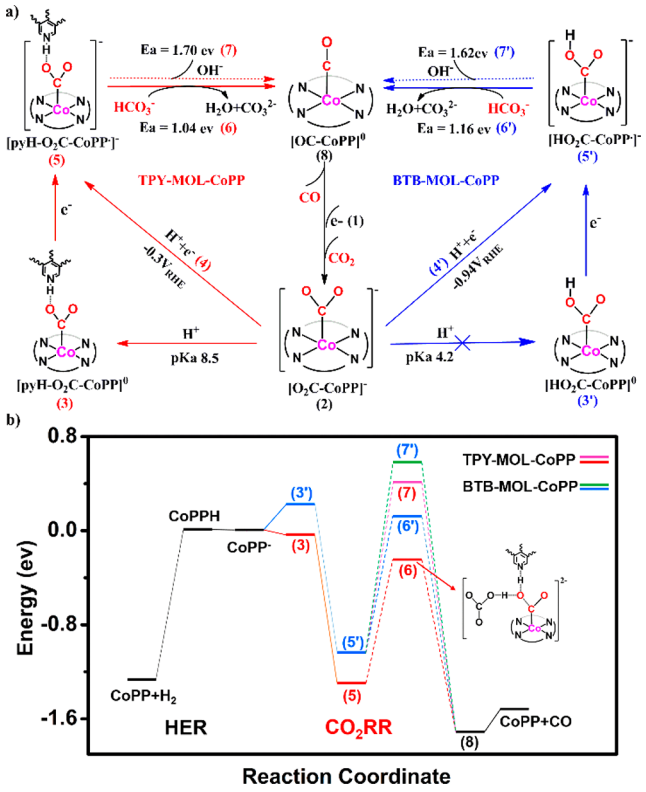

Figure 8. (a) Catalytic cycle of the CO_2RR by TPY-MOL-CoPP and BTB-MOL-CoPP. The pK_a values and redox potentials from DFT calculations are also shown. (b) Calculated energy profiles for HER and CO_2RR processes of TPY-MOL-CoPP and BTB-MOL-CoPP.

restricted movement of the preassembled pyridine decreases the entropy loss to act as a better base, a ubiquitous feature in enzymatic catalysis. Consistent with this conjecture, the addition of 2,6-lutidine, a strong but noncoordinating base, to the solution did not promote the CO_2RR selectivity of the BTB-MOL-CoPP catalyst (Figure 4a). A complete suppression of the translational and rotational entropy of the pyridine moiety leads to a calculated pK_a of 16.6 that favors the protonated form at neutral pH, and the free pyridine gives a pK_a of 4.2. In our assembly, the CoPP moiety has some flexibility to accommodate the CO_2 substrate so that the entropy term is not completely suppressed. As a result, we remove only half of the translational entropy of the pyridine to estimate the pK_a value (8.5) of the $[pyH\text{-}O_2C\text{-}CoPP]^{0/-}$ intermediate. We also note the possibility of the reduction of protonated terpyridine during the catalytic cycle, which may further facilitate the second electron injection.

We estimated the rate of the second electron transfer following Marcus theory. The electron transfer barrier is assessed by calculating the energies of the reduced or oxidized species at the optimized geometries before and after electron transfer (four energies in total). Cross-linking the four points gives an estimation of the cross point in Marcus theory used to obtain the energy barrier (Figure S24). We found that the barrier of the electron transfer is low (approaching 0.01 eV for $[HO_2C\text{-}CoPP]^{0/-}$ and 0.1 eV for $[pyH\text{-}O_2C\text{-}CoPP]^{0/-}$), suggesting fast electron transfers.

As a result, the cleavage of the C−O bond must be the rate-determining step (RDS). Consistent with this, we observed a large H/D kinetic isotope effect (KIE) for j_{CO} in CO_2RR experiments using $NaDCO_3/CO_2/D_2O$ vs $NaHCO_3/CO_2/H_2O$ solutions. The large j_{CO-H}/j_{CO-D} values of 20 for TPY-MOL-CoPP and 14.4 for BTB-MOL-CoPP suggest the potential involvement of H-tunneling in the RDS. We calculated the energy barriers of the C−O breaking steps for TPY-MOL-CoPP and the BTB-MOL-CoPP. The transition state was found by optimizing the structure with a progressively elongated C−O bond length until bond cleavage (Figures S25−S28). Because our experimental kinetics measurements indicate an additional HCO_3^--assisted pathway, we also calculated the energy barrier with a concerted proton transfer from HCO_3^- to the hydroxy group in the C−O cleavage. We obtained an activation energy of 1.70 eV for TPY-MOL-CoPP in the direct C−O bond cleavage pathway and an activation energy of 1.03 eV in the HCO_3^- assisted pathway (Figure 8b), agreeing with the experimental rate law. The transition state of the direct C−O cleavage has a C−O bond length of 2.8 Å, and the transition state of the HCO_3^--assisted pathway has a C−O bond length of 2.4 Å. Similarly, the activation energy of BTB-MOL-CoPP is 1.16 eV for the HCO_3^--assisted pathway and 1.62 eV for the direct bond cleavage pathway (Figure 8b).

Rate Law Based on the Catalytic Cycle. On the basis of the catalytic cycle with the C−O bond cleavage as the RDS, we can derive the rate laws. For the reaction catalyzed by TPY-MOL-CoPP, $[pyH\text{-}O_2C\text{-}CoPP]^0$ is in equilibrium with $[H\text{-}CoPP]^0$, $[CoPP]^-$, $[O_2C\text{-}CoPP]^-$, and $[HO_2C\text{-}CoPP]^0$ (which can be ignored because $[HO_2C\text{-}CoPP]^0 \ll [pyH\text{-}O_2C\text{-}CoPP]^0$). As a result,

$$[pyH\text{-}O_2C\text{-}CoPP]^0 = \frac{[CO_2]}{[CO_2] + K_1 + \frac{K_2}{[H^+]} + \frac{K_3[CO_2]}{[H^+]}}[Co] \quad (8)$$

where [Co] is the total number of Co sites and K's are the equilibrium constants. From the theoretical calculation, we can obtain $K_1 = 10^{-1.85}$ M, $K_2 = 10^{-8.85}$ M^2, and $K_3 = 10^{-8.5}$.

There are two paths for the C−O bond cleavage (the bicarbonate-assisted path and the direct path), leading to the following rate law:

$$\frac{j_{CO}}{[Co]} = (k_1[HCO_3^-] + k_2)\frac{[pyH - O_2C - CoPP]^0}{[Co]} = (k_1[HCO_3^-] + k_2)\frac{[CO_2]}{\left([CO_2] + K_1 + \frac{K_2}{[H^+]} + \frac{K_3[CO_2]}{[H^+]}\right)} \quad (9)$$

This rate law matches the one from the experimental data when $K_1 \gg K_2/[H^+]$ and $K_3[CO_2]/[H^+]$. The calculated equilibrium constants are different as compared to those from experimental fitting, mainly because of the difficulty in accurately estimating the entropy term of the pyridine moiety.

For the BTB-MOL-CoPP catalyst, because the formation of $[HO_2C\text{-}CoPP]^0$ is not favorable and a proton-coupled electron transfer pathway is more likely, we consider the $[O_2C\text{-}CoPP]^-$ concentration in equilibrium with $[H\text{-}CoPP]^0$, $[CoPP]^-$, and $[HO_2C\text{-}CoPP]^0$.

$$[O_2C\text{-}CoPP]^- = \frac{[CO_2]}{[CO_2] + K_1' + K_2'[H^+] + K_3'[CO_2][H^+]}[Co] \quad (10)$$

Again, considering the two paths for the C−O bond cleavage, we can obtain a rate law that matches the one from the experimental data:

DOI: 10.1021/jacs.9b09227
J. Am. Chem. Soc. 2019, 141, 17875−17883

$$\frac{j_{CO}}{[Co]} = (k_1'[HCO_3^-] + k_2')\frac{[O_2C - CoPP]^-}{[Co]} = (k_1'[HCO_3^-] + k_2') \times \frac{[CO_2]}{([CO_2] + K_1' + K_2'[H^+] + K_3'[CO_2][H^+])} \quad (11)$$

From the theoretical calculation, we obtain $K_1' = 0.44$ M, $K_2' = 10^{6.65}$, and $K_3' = 10^{4.2}$ M^{-1} ($K_1' \approx K_2'[H^+] \gg K_3'[CO_2][H^+]$). These slightly deviate from the results from the experimental fitting, but the general trend is reasonable.

Figure 8 shows the main path of the CO_2RR process catalyzed by CoPP (Figure 8a, Figures S29 and S30) together with the energy profile of the key steps (Figure 8b) based on the above analyses. The $1e^-$ reduction of CoPP is followed by CO_2 adsorption and protonation to form $[HO_2C\text{-}CoPP]^0$, in competition with the formation of $[H\text{-}CoPP]^0$ that leads to HER. The preassembled pyridine moiety stabilizes the $[pyH\text{-}O_2C\text{-}CoPP]^0$ species to favor the CO_2RR path over the HER path in TPY-MOL-CoPP, as shown by the different energies of **3** and **3′** as compared to that of $[H\text{-}CoPP]^0$ in Figure 8b. The RDS in the CO_2RR is the cleavage of the C−O bond after the second electron injection. A HCO_3^--assisted process decreases the energy barrier in the RDS (**6** vs **7** and **6′** vs **7′** in Figure 8b). The pyridinium moiety also changes the energy of the transition state. The release of CO from $[OC\text{-}CoPP]^0$ regenerates the CoPP for catalytic turnover. The pyridinium moiety thus lowers the energy barrier both for CO_2 adsorption and for C−O bond cleavage to promote the CO_2RR.

CONCLUSIONS

We constructed a catalytic pocket with a CoPP center and a pyridine moiety on a MOL layer for cooperative adsorption and activation of CO_2 for electrochemical CO_2 reduction. The TPY-MOL-CoPP catalyst shows an enhanced CO/H_2 selectivity of 11.8 as compared to a CO/H_2 selectivity of 2.7 for BTB-MOL-CoPP without pyridine. This work highlights unique opportunities in using MOLs as a tunable platform to construct catalytic sites with secondary interactions to enhance product selectivity and to provide mechanistic insights into important electrocatalytic processes.

ASSOCIATED CONTENT

Supporting Information

The Supporting Information is available free of charge on the ACS Publications website at DOI: 10.1021/jacs.9b09227.

Experimental details, spectroscopic characterization, DFT calculations, and COMSOL simulation (PDF)

AUTHOR INFORMATION

Corresponding Author

*wangchengxmu@xmu.edu.cn

ORCID

Cheng Wang: 0000-0002-7906-8061

Wenbin Lin: 0000-0001-7035-7759

Author Contributions

§These authors contributed equally.

Notes

The authors declare no competing financial interest.

ACKNOWLEDGMENTS

We acknowledge funding support from the National Natural Science Foundation and Ministry of Science and Technology of P. R. China (NSFC21671162, 2016YFA0200702, and NSFC21721001).

REFERENCES

(1) Diercks, C. S.; Liu, Y.; Cordova, K. E.; Yaghi, O. M. The role of reticular chemistry in the design of CO_2 reduction catalysts. *Nat. Mater.* **2018**, *17*, 301.

(2) Hu, X. M.; Ronne, M. H.; Pedersen, S. U.; Skrydstrup, T.; Daasbjerg, K. Enhanced Catalytic Activity of Cobalt Porphyrin in CO_2 Electroreduction upon Immobilization on Carbon Materials. *Angew. Chem., Int. Ed.* **2017**, *56*, 6468.

(3) Nam, D. H.; Bushuyev, O. S.; Li, J.; De Luna, P.; Seifitokaldani, A.; Dinh, C. T.; Garcia de Arquer, F. P.; Wang, Y.; Liang, Z.; Proppe, A. H.; Tan, C. S.; Todorovic, P.; Shekhah, O.; Gabardo, C. M.; Jo, J. W.; Choi, J.; Choi, M. J.; Baek, S. W.; Kim, J.; Sinton, D.; Kelley, S. O.; Eddaoudi, M.; Sargent, E. H. Metal-Organic Frameworks Mediate Cu Coordination for Selective CO_2 Electroreduction. *J. Am. Chem. Soc.* **2018**, *140*, 11378.

(4) Elgrishi, N.; Chambers, M. B.; Wang, X.; Fontecave, M. Molecular polypyridine-based metal complexes as catalysts for the reduction of CO_2. *Chem. Soc. Rev.* **2017**, *46*, 761.

(5) Kang, P.; Cheng, C.; Chen, Z.; Schauer, C. K.; Meyer, T. J.; Brookhart, M. Selective electrocatalytic reduction of CO_2 to formate by water-stable iridium dihydride pincer complexes. *J. Am. Chem. Soc.* **2012**, *134*, 5500.

(6) Hod, I.; Sampson, M. D.; Deria, P.; Kubiak, C. P.; Farha, O. K.; Hupp, J. T. Fe-Porphyrin-Based Metal−Organic Framework Films as High-Surface Concentration, Heterogeneous Catalysts for Electrochemical Reduction of CO_2. *ACS Catal.* **2015**, *5*, 6302.

(7) Takeda, H.; Cometto, C.; Ishitani, O.; Robert, M. Electrons, Photons, Protons and Earth-Abundant Metal Complexes for Molecular Catalysis of CO_2 Reduction. *ACS Catal.* **2017**, *7*, 70.

(8) Mariano, R. G.; McKelvey, K.; White, H. S.; Kanan, M. W. Selective increase in CO_2 electroreduction activity at grain-boundary surface terminations. *Science* **2017**, *358*, 1187.

(9) Albo, J.; Beobide, G.; Castaño, P.; Irabien, A. Methanol electrosynthesis from CO_2 at Cu_2O/ZnO prompted by pyridine-based aqueous solutions. *Journal of CO_2 Utilization* **2017**, *18*, 164.

(10) Barton Cole, E.; Lakkaraju, P. S.; Rampulla, D. M.; Morris, A. J.; Abelev, E.; Bocarsly, A. B. Using a One-Electron Shuttle for the Multielectron Reduction of CO_2 to Methanol: Kinetic, Mechanistic, and Structural Insights. *J. Am. Chem. Soc.* **2010**, *132*, 11539.

(11) Barton, E. E.; Rampulla, D. M.; Bocarsly, A. B. Selective solar-driven reduction of CO_2 to methanol using a catalyzed p-GaP based photoelectrochemical cell. *J. Am. Chem. Soc.* **2008**, *130*, 6342.

(12) Bocarsly, A. B.; Gibson, Q. D.; Morris, A. J.; L'Esperance, R. P.; Detweiler, Z. M.; Lakkaraju, P. S.; Zeitler, E. L.; Shaw, T. W. Comparative Study of Imidazole and Pyridine Catalyzed Reduction of Carbon Dioxide at Illuminated Iron Pyrite Electrodes. *ACS Catal.* **2012**, *2*, 1684.

(13) Fang, Y.; Flake, J. C. Electrochemical Reduction of CO_2 at Functionalized Au Electrodes. *J. Am. Chem. Soc.* **2017**, *139*, 3399.

(14) Sharma, P. P.; Wu, J.; Yadav, R. M.; Liu, M.; Wright, C. J.; Tiwary, C. S.; Yakobson, B. I.; Lou, J.; Ajayan, P. M.; Zhou, X. D. Nitrogen-Doped Carbon Nanotube Arrays for High-Efficiency Electrochemical Reduction of CO_2: On the Understanding of Defects, Defect Density, and Selectivity. *Angew. Chem., Int. Ed.* **2015**, *54*, 13701.

(15) Pan, Y.; Lin, R.; Chen, Y.; Liu, S.; Zhu, W.; Cao, X.; Chen, W.; Wu, K.; Cheong, W. C.; Wang, Y.; Zheng, L.; Luo, J.; Lin, Y.; Liu, Y.; Liu, C.; Li, J.; Lu, Q.; Chen, X.; Wang, D.; Peng, Q.; Chen, C.; Li, Y. Design of Single-Atom Co-N5 Catalytic Site: A Robust Electrocatalyst for CO_2 Reduction with Nearly 100% CO Selectivity and Remarkable Stability. *J. Am. Chem. Soc.* **2018**, *140*, 4218.

(16) Dridi, H.; Comminges, C.; Morais, C.; Meledje, J. C.; Kokoh, K. B.; Costentin, C.; Saveant, J. M. Catalysis and Inhibition in the Electrochemical Reduction of CO_2 on Platinum in the Presence of Protonated Pyridine. New Insights into Mechanisms and Products. *J. Am. Chem. Soc.* **2017**, *139*, 13922.

(17) Lim, C. H.; Holder, A. M.; Hynes, J. T.; Musgrave, C. B. Reduction of CO_2 to methanol catalyzed by a biomimetic organo-hydride produced from pyridine. *J. Am. Chem. Soc.* **2014**, *136*, 16081.
(18) Senftle, T. P.; Lessio, M.; Carter, E. A. The Role of Surface-Bound Dihydropyridine Analogues in Pyridine-Catalyzed CO_2 Reduction over Semiconductor Photoelectrodes. *ACS Cent. Sci.* **2017**, *3*, 968.
(19) Yan, Y.; Zeitler, E. L.; Gu, J.; Hu, Y.; Bocarsly, A. B. Electrochemistry of aqueous pyridinium: exploration of a key aspect of electrocatalytic reduction of CO_2 to methanol. *J. Am. Chem. Soc.* **2013**, *135*, 14020.
(20) Keith, J. A.; Carter, E. A. Theoretical Insights into Electrochemical CO_2 Reduction Mechanisms Catalyzed by Surface-Bound Nitrogen Heterocycles. *J. Phys. Chem. Lett.* **2013**, *4*, 4058.
(21) Campbell, M. G.; Liu, S. F.; Swager, T. M.; Dinca, M. Chemiresistive Sensor Arrays from Conductive 2D Metal-Organic Frameworks. *J. Am. Chem. Soc.* **2015**, *137*, 13780.
(22) Zhao, M.; Lu, Q.; Ma, Q.; Zhang, H. Two-Dimensional Metal-Organic Framework Nanosheets. *Small Methods* **2017**, *1*, 1600030.
(23) Cao, L.; Lin, Z.; Peng, F.; Wang, W.; Huang, R.; Wang, C.; Yan, J.; Liang, J.; Zhang, Z.; Zhang, T.; Long, L.; Sun, J.; Lin, W. Self-Supporting Metal-Organic Layers as Single-Site Solid Catalysts. *Angew. Chem., Int. Ed.* **2016**, *55*, 4962.
(24) Wang, T.; Zeng, Z.; Cao, L.; Li, Z.; Hu, X.; An, B.; Wang, C.; Lin, W. A Dynamically Stabilized Single-Nickel Electrocatalyst for Selective Reduction of Oxygen to Hydrogen Peroxide. *Chem. - Eur. J.* **2018**, *24*, 17011.
(25) Zhao, S.; Wang, Y.; Dong, J.; He, C.-T.; Yin, H.; An, P.; Zhao, K.; Zhang, X.; Gao, C.; Zhang, L.; Lv, J.; Wang, J.; Zhang, J.; Khattak, A. M.; Ali Khan, N.; Wei, Z.; Zhang, J.; Liu, S.; Zhao, H.; Tang, Z. Ultrathin metal-organic framework nanosheets for electrocatalytic oxygen evolution. *Nat. Energy* **2016**, *1*, 16184.
(26) Shi, W.; Cao, L.; Zhang, H.; Zhou, X.; An, B.; Lin, Z.; Dai, R.; Li, J.; Wang, C.; Lin, W. Surface Modification of Two-Dimensional Metal-Organic Layers Creates Biomimetic Catalytic Microenvironments for Selective Oxidation. *Angew. Chem., Int. Ed.* **2017**, *56*, 9704.
(27) Monti, D.; Ottolina, G.; Carrea, G.; Riva, S. Redox reactions catalyzed by isolated enzymes. *Chem. Rev.* **2011**, *111*, 4111.
(28) Wang, Z. J.; Clary, K. N.; Bergman, R. G.; Raymond, K. N.; Toste, F. D. A supramolecular approach to combining enzymatic and transition metal catalysis. *Nat. Chem.* **2013**, *5*, 100.
(29) Lin, S.; Nichols, E. M.; Diercks, C. S.; Zhang, Y.-B.; Kornienko, N.; Zhao, Y.; Paris, A. R.; Kim, D.; Yang, P.; Yaghi, O. M.; Chang, C. J. Covalent organic frameworks comprising cobalt porphyrins for catalytic CO_2 reduction in water. *Science* **2015**, *349*, 1208.
(30) Diercks, C. S.; Lin, S.; Kornienko, N.; Kapustin, E. A.; Nichols, E. M.; Zhu, C.; Zhao, Y.; Chang, C. J.; Yaghi, O. M. Reticular Electronic Tuning of Porphyrin Active Sites in Covalent Organic Frameworks for Electrocatalytic Carbon Dioxide Reduction. *J. Am. Chem. Soc.* **2018**, *140*, 1116.
(31) Kornienko, N.; Zhao, Y.; Kley, C. S.; Zhu, C.; Kim, D.; Lin, S.; Chang, C. J.; Yaghi, O. M.; Yang, P. Metal-organic frameworks for electrocatalytic reduction of carbon dioxide. *J. Am. Chem. Soc.* **2015**, *137*, 14129.
(32) Singh, M. R.; Kwon, Y.; Lum, Y.; Ager, J. W., III; Bell, A. T. Hydrolysis of Electrolyte Cations Enhances the Electrochemical Reduction of CO_2 over Ag and Cu. *J. Am. Chem. Soc.* **2016**, *138*, 13006.
(33) Dunwell, M.; Yang, X.; Setzler, B. P.; Anibal, J.; Yan, Y.; Xu, B. Examination of Near-Electrode Concentration Gradients and Kinetic Impacts on the Electrochemical Reduction of CO_2 using Surface-Enhanced Infrared Spectroscopy. *ACS Catal.* **2018**, *8*, 3999.
(34) Tobias, C. W.; Eisenberg, M.; Wilke, C. R. Diffusion and convection in electrolysis-a theoretical review. *J. Electrochem. Soc.* **1952**, *99*, 359C.
(35) Singh, M. R.; Clark, E. L.; Bell, A. T. Effects of electrolyte, catalyst, and membrane composition and operating conditions on the performance of solar-driven electrochemical reduction of carbon dioxide. *Phys. Chem. Chem. Phys.* **2015**, *17*, 18924.
(36) Gottle, A. J.; Koper, M. T. M. Determinant Role of Electrogenerated Reactive Nucleophilic Species on Selectivity during Reduction of CO_2 Catalyzed by Metalloporphyrins. *J. Am. Chem. Soc.* **2018**, *140*, 4826.
(37) Gottle, A. J.; Koper, M. T. M. Proton-coupled electron transfer in the electrocatalysis of CO_2 reduction: prediction of sequential vs. concerted pathways using DFT. *Chem. Sci.* **2017**, *8*, 458.
(38) Leung, K.; Nielsen, I. M. B.; Sai, N.; Medforth, C.; Shelnutt, J. A. Cobalt-porphyrin catalyzed electrochemical reduction of carbon dioxide in water. 2. Mechanism from first principles. *J. Phys. Chem. A* **2010**, *114*, 10174.
(39) de Groot, M. T.; Koper, M. T. Redox transitions of chromium, manganese, iron, cobalt and nickel protoporphyrins in aqueous solution. *Phys. Chem. Chem. Phys.* **2008**, *10*, 1023.
(40) Shen, J.; Kortlever, R.; Kas, R.; Birdja, Y. Y.; Diaz-Morales, O.; Kwon, Y.; Ledezma-Yanez, I.; Schouten, K. J.; Mul, G.; Koper, M. T. Electrocatalytic reduction of carbon dioxide to carbon monoxide and methane at an immobilized cobalt protoporphyrin. *Nat. Commun.* **2015**, *6*, 8177.

DOI: 10.1021/jacs.9b09227
J. Am. Chem. Soc. 2019, 141, 17875−17883